Experimental analysis of the effects of wrinkles in the radius of curvature of L-shaped carbon-epoxy specimens on unfolding failure

Pierre Journoud, Christophe Bouvet, Bruno Castanié, Léon Ratsifandrihana

Experimental analysis of the effects of wrinkles in the radius of curvature of L-shaped carbon-epoxy specimens on unfolding failure

P. Journoud [a,b], C. Bouvet [a], B. Castanié [a,*], L. Ratsifandrihana [b]

[a] Institut Clément Ader, Université de Toulouse, CNRS UMR 5312 – INSA – ISAE-SUPAERO – IMT Mines Albi – UPS – 3 rue Caroline Aigle, 31400 Toulouse, France
[b] Segula Aerospace & Defence, Segula Technologie – immeuble EQUINOX – bat. 1, 24 Boulevard Déodat de Severac, 31770 Colomiers, France

Keywords:
Carbon fibres
Damage tolerance
Defects
Delamination
Fracture
Mechanical testing

A B S T R A C T

An experimental study has been carried out to describe the evolution of the failure load relative to the maximum misalignment angle of curved carbon–epoxy laminates with out-of-plane wrinkle defects for a large range of misalignments. L-angle specimens with different levels of fibre wrinkling were manufactured and tested in four-point bending tests. Digital Image Correlation (DIC) and infrared thermography were used to monitor the tests. They allowed the stress concentrations induced by the wrinkles to be identified, together with their influences on the failure load of the sample. In most cases, increases in wrinkling levels led to decreases in failure loads.

1. Introduction

In the current context of global warming, composite materials offer an interesting alternative to metallic materials, thanks to their high strength to weight ratios, and enable efficient lightweight structures to be designed [1]. The range of materials and architectures they make possible is very wide but all are closely linked to the manufacturing processes [2]. Composite laminates are not restricted to flat components but can be manufactured with complex geometries. Some parts, such as L-angle composites, even present high curvature and are used, in particular, at the junction between two perpendicular parts, especially for "clips" in stiffened aeronautical structures, where they are subjected to bending moments, which induce out-of-plane stresses. Thus, laminate composites with a high curvature are more prone to defects during their manufacture. These particularly concern fibre wrinkling but voids, corner thickening or corner thinning can also occur [3].

Potter et al. [4] showed that waviness may already be present in the uncured prepregs. This means that it could result from the production process, the transport or the storage of the materials. Nevertheless, most of the time, it was found to be induced by the manufacturing process. The production of defect-free composites is difficult, especially when the part does not have a conventional shape and involves one or more directions and degrees of curvature [5]. Hassan et al. [3] have reviewed the manufacturing defects occurring in complex shaped laminated composites. Voids, delaminations, fibre wrinkling, resin accumulation, corner thickening and corner thinning are the most common defects appearing during the manufacture of laminated composite structures with complex geometry [3,6,7].

Kulkarni et al. [8] and Hassan [3] summarised numerous sources of fibre waviness. Some were inherent in the laminated composite: the stacking sequence [9,10], the difference of thermal expansion coefficients between the fibres and the matrix [11], the critical limb length [12], the inter-ply shear stress or the through-thickness compaction [13,14]. Other works have focused on the wrinkling sources in relation with the interactions between the part and the mould: the difference of thermal expansion coefficients [15,16], the proportion of 0° plies and the size of the corner radius of the mould [17]. Some works concern the influence of external parameters on the development of wrinkles within the composite: the shape of the mould [18–20], the consolidation in an autoclave or out-of-autoclave [18,21–23].

The presence of wrinkles within a laminate needs to be characterised in order to be compared and classified. The two main parameters that characterise the severity of wrinkles are: the maximum wrinkle angle θ_{max}, which corresponds to the maximum angle formed by the wrinkling fibres in comparison to their initial direction [24–27], and the A/L ratio, which corresponds to the ratio of the amplitude (A) of the wrinkle to its wavelength (L) (Fig. 1) [27,28]. In addition, some authors have paid attention to the ratio of wavelength, which corresponds to the number of plies affected by the wrinkles relative to the total number of plies of the stacking sequence [29]. To finish, the location of wrinkling regions in the thickness of the specimen and the different types of distribution (single waves, stochastic distributed waves, or in-phase distributed

* Corresponding author.
E-mail address: bruno.castanie@insa-toulouse.fr (B. Castanié).

https://doi.org/10.1016/j.compositesa.2022.106975

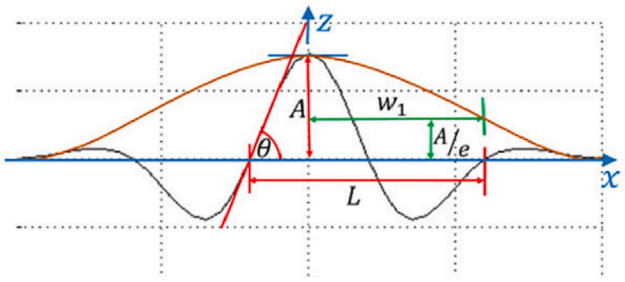

Fig. 1. Measurement of θ_{max} and A/L ratio to characterise the severity of wrinkles [27]. (For interpretation of the references to colour in this figure legend, the reader is referred to the web version of this article.)

waves) of the wrinkles through the thickness of a composite layup and the distribution of the wave amplitude (graduated, uniform) through the thickness have also been used to characterise wrinkling [29].

It is recognised that wrinkles have significant influence on the mechanical properties of laminated composites and on their strength. Most of the works found in the literature focus on the effect of out-of-plane wrinkles on the strength of flat specimens under compression tests [24,27,30–32]. Amongst these studies, Hsiao and Daniel [31] demonstrate that the failure strength is more sensitive to the wrinkles than the stiffness, especially when the A/L ratio is small. Adams and Hyer [30] found a strength reduction in compression of between 1% and 36% for wrinkles with a maximum misalignment angle of between 3° and 17°. This corroborates the work of Mukhopadhyay et al. [24], who studied three levels of misalignment (5.6°, 9.9° and 11.4°) and obtained a loss of 18% of the strength in compression for the lowest level of misalignment and 34% for the most pronounced wrinkles (9.9° and 11.4°). All of these studies focused on the effect of wrinkles on the mechanical properties of a planar laminar composite. To the best of our knowledge, only Xu et al. [33] and Hu et al. [34] have studied the effects of wrinkles in curved composite specimens under four-point bending tests and only for a limited number of differently wrinkled specimens. Xu et al. [33] manufactured L-angle specimens with a maximum misalignment angle of 18° and they concluded on a reduction of the out-of-plane tensile stress of 16%. Hu et al. [34] concluded that the location and amplitudes of wrinkles had a significant influence on the mechanical response of the specimen, which could lead to a reduction of 30% to 40% of the failure load.

An analysis of the literature shows that there are few studies on the effect of wrinkle defects in the radius of curvature on the mechanical properties, despite the fact that wrinkling is the most common defect on a curved specimen. Moreover, the failure of wrinkled specimens is poorly understood and the maximum misalignment angle does not seem to fully characterise the failure of curved specimens. Therefore, it appears important to produce a larger number of wrinkled specimens with a broad range of different maximum misalignment angles. For this study, 42 specimens were produced by means of the two hand layup strategies described in Section 2.2. The wrinkles were characterised by the maximum misalignment angle compared to the reference surface, which ranged from 5.3° to 83.3° (Section 3.1). The damage scenarios of three levels of wrinkles (1.5 ± 2°, 26 ± 2° and 45 ± 2°) are detailed in Section 3.2 and a general comparison between the failure loads and evolution of wrinkling levels is made in Section 3.4. In Section 4, conclusions are drawn based on the above.

2. Materials and methods

This first part focuses on an experimental study of the method for manufacturing specimens, the test setups and the instrumentation used during the test. Section 2.1 contains all relevant information about the material used for the study. Section 2.2 describes how the pre-impregnated materials were laid up by hand and how the wrinkles were introduced into the radius of curvature of L-angle specimens. Section 2.3 provides details concerning the experimental setups. To finish, Section 2.4 refers to the instrumentation used during the four-point bending test.

2.1. Materials

The tests were performed on L-Shaped CFRP specimens. The fibres and epoxy resin were respectively T700 and M21 (Hexcel Composites Company). The layup used was $[45_2/\text{-}\,45_2/90_2/0_2]_S$, so the 16 plies had a total theoretical thickness of 4.125 mm. This type of stacking with ± 45° plies as external plies is due to buckling considerations. It maximize the buckling load and is currently used in aeronautics. By convention, the layer orientations mentioned in the stacking are always expressed from the inner layer surface to the outer layer surface. The longitudinal direction of fibres is represented in Fig. 2. The specimens have an arm length of 113 mm, a width of 20 mm and an inner radius of 5.16 mm (Fig. 2). The laminate stacks were prepared in a controlled atmosphere and compaction was carried out for 12 h using a vacuum pump. The curing process was conducted in an autoclave at 180 °C for 120 min, with a pressure maintained at 7 bar. Experimentally, the average of thickness of the specimens were measured equal to 4.1 ± 0.1 mm in the flat part of the arm. In the radius of curvature, the thickness is not constant and depends of the level of misalignment angle. Therefore, it was not measured.

2.2. Manufacturing method

To manufacture specimens with wrinkles in the (xz) coordinate system (Fig. 2), two geometries of mould were used. A convex mould (Fig. 3 a.) to produce specimens with limited defects and a concave mould (Fig. 3 b.) to make samples with wrinkle defects in the radius of curvature. With the concave mould, two hand layup strategies were considered in order to produce specimens with different levels of wrinkles, following the method proposed by Hu et al. [34]. In the first one, plies were directly stacked in the mould by hand with compaction, enabling parts to be made without defects. The second strategy involved stacking some or all of the layers (Fig. 4) on a flat surface first and then moving them into the mould. This second method promoted the appearance of wrinkles in the radius of curvature. The different maximum angles of misalignment created in the specimens were obtained by mixing these two strategies. The number of layers with wrinkles and the maximum angle of misalignment increased with the number of plies stacked with the second method.

Seven types of specimens, using different ratios of the two strategies, were manufactured for this study and are summarised in Fig. 4. EM specimens (1, 2 and 3) were made using the first strategy exclusively. The concave mould was used for the EM-1 and EM-2 samples. Convex moulds were exclusively used for the EM-3 specimens, the aim being to

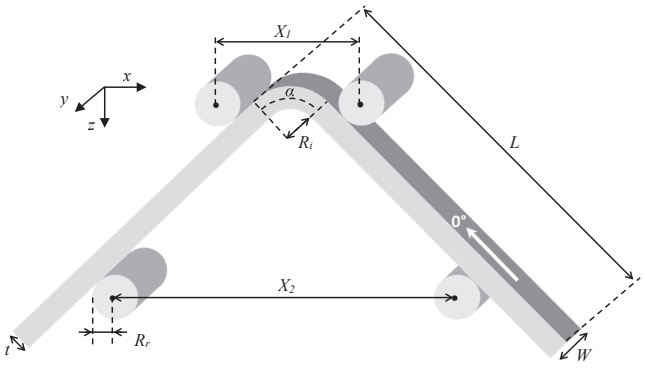

Fig. 2. Dimensions and characteristic parameters of the four-point bending test on L-shaped specimen.

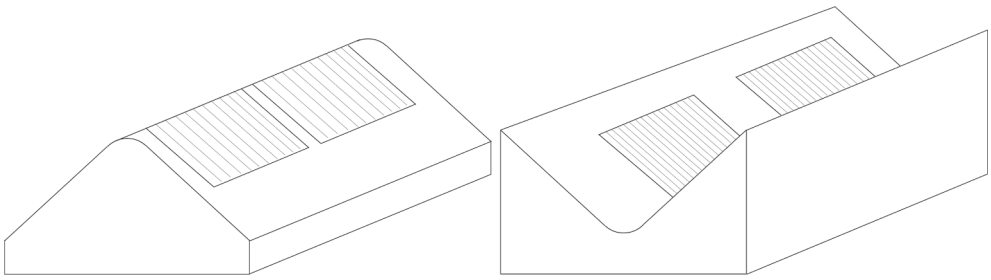

Fig. 3. a. Convex mould, b. concave mould used for manufacturing.

EM-1	EM-2	EM-3	EP-1/8	EP-1/4	EP-1/2	EP-1
45	45	45	45	45	45	45
45	45	45	45	45	45	45
-45	-45	-45	-45	-45	-45	-45
-45	-45	-45	-45	-45	-45	-45
90	90	90	90	90	90	90
90	90	90	90	90	90	90
0	0	0	0	0	0	0
0	0	0	0	0	0	0
0	0	0	0	0	0	0
0	0	0	0	0	0	0
90	90	90	90	90	90	90
90	90	90	90	90	90	90
-45	-45	-45	-45	-45	-45	-45
-45	-45	-45	-45	-45	-45	-45
45	45	45	45	45	45	45
45	45	45	45	45	45	45

Plies stacked on a flat surface before being introduced into the mould

Fig. 4. Strategies of hand layup used for the different specimens manufactured. (For interpretation of the references to colour in this figure legend, the reader is referred to the web version of this article.)

produce L-angle specimens with the lowest possible angle of misalignment. EP samples were stacked by using a combination of both the strategies presented. The proportion of plies stacked with the second method has been outlined in red on Fig. 4. For instance, all sixteen plies of EP-1 were stacked with the second strategy. For the EP-1/8 the first seven plies ($[45_2/-45_2/90_2/0]$) were stacked directly on the concave mould. These aluminium plates were exclusively used for the bending of plies of EP-1/4 and EP-1/8. For the other specimens (EP-1 and EP-1/2) the number of plies was sufficient to avoid their use and to localise the wrinkles in the part of the radius of curvature. To finish, the last seven

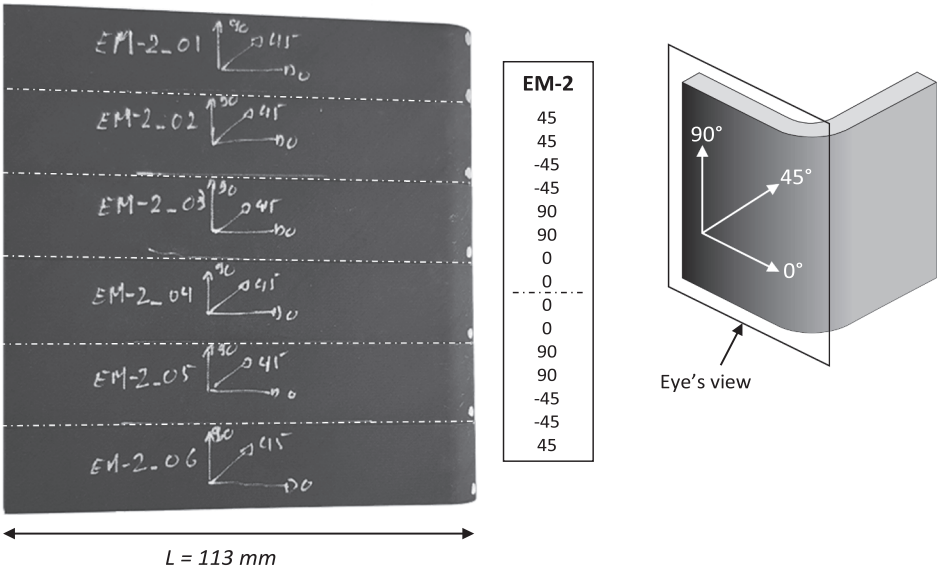

Fig. 5. Sample EM-2 cuts into six specimens after curing.

plies were stacked on the concave mould. It is noteworthy that, for each specimen, pressure was applied every two plies with a vacuum bag for fifteen minutes in order to avoid voids.

The dimensions of the pre-impregnated material used to manufacture each sample were 150 mm × 250 mm. After curing, each sample was cut (along the discontinuous axis of Fig. 5) into six specimens with an arm length of 113 mm and a width of 20 mm. Therefore, a total of 42 specimens shared among 5 manufacturing strategies of were tested in this study.

2.3. Four-point bending test

The aim of the four-point bending test was to induce a pure bending moment at the curved section by the displacement of the two upper cylindrical rollers, while the two lower ones stayed fixed. The geometry of the L-angle specimens was studied by Charrier et al. [35] to minimise the out-of-plane shear stress and maximise the out-of-plane tensile stress in the area of the radius of curvature. The setup of the four-point bending tests is illustrated in Fig. 6. The characteristic parameters (Table 1) were the same as used in the work of Charrier et al. [35,36] and in a previous study [37] on the numerical simulation of four-point bending tests on specimens without defects. The four-point bending tests were conducted on an INSTRON 4466 100 kN traction machine with a specific 10 kN load cell. The specimens were subjected to displacement at a rate of 2 mm/min until the end of the tests.

2.4. Monitoring

The tests were multi-instrumented (Fig. 6). First, a linear variable differential transducer (LVDT) positioned on the upper support bar was used. Then, a fine painted speckle pattern was applied on one side of the specimen to perform 2D Digital Image Correlation (DIC). The camera used to record the section of interest, the section of the radius of curvature, had a resolution of 5 Mpixels. In addition, a Télops Fast M3K infrared thermography camera was used on the other side of the specimens with a resolution of 193 × 132 pixels. This was used to evaluate the temperature field and the heat released by the failure of the specimen, and to localise the damage.

3. Experimental results of four-point bending tests on L-angle specimens with defects

3.1. Maximum misalignment angle

The free edges of the specimens were captured after polishing and the exact shape of the wrinkle were drawn using a set of discretization points. Then by using a finite element software (Abaqus), the maximum misalignment angle (noted θ_{max}) was measured relative to a reference surface, which corresponded to the surface in contact with the mould.

Table 1
Nominal specimen dimensions and characteristic parameters of the experimental device for the four-point bending test.

Thickness	Length	Width	Inner radius	Radius of cylindrical bars	Loading bars	Support bars
t (mm)	L (mm)	W (mm)	R_i (mm)	R_r (mm)	X_1 (mm)	X_2 (mm)
4.125	113	20	5.16	7.5	30	66

This parameter was chosen to characterise the criticality of the wrinkle defects for each specimen. The misalignment angle θ_{max} was calculated from the experimental data as the difference between the maximum misalignment angle corresponding to the wrinkle α_1 and the maximum angle corresponding to the reference surface of specimen α_2 (Fig. 7). The measurement had a precision of ±2°. It was quantitatively estimated by analysing the refinement of the mesh created by the discretization points. The value of misalignment for a specimen corresponded to the average of the maximum misalignment angles on both sides of the specimen (Fig. 5).

Examples of wrinkles introduced with the different strategies described in Section 2.2, are shown in Fig. 8. The wrinkled areas are localised by a red circle and the maximum misalignment angle by a red arrow. Fig. 9 presents the distribution of the mean values of the maximum misalignment angle measured and the length of pre-delamination for each batch of specimens, with standard deviation. We remind that the EM specimens were made exclusively by directly draping the pre-impregnated material on the mould. EM-1 and EM-2 were manufactured in a concave mould and only the EM-3 specimen was made with a convex mould. The EM-1 specimens had the lowest misalignment angle, with an average of 2.1° and excellent repeatability. The EM-3 specimens had an average value of misalignment angle of 11.1° and, unlike all other specimens of this study, had a reference surface that was the internal one due to the convexity of the mould. Consequently, the wrinkles developed on the upper part of the sample (Fig. 8, EM-3-12°). The EM-2 specimens had an average maximum misalignment angle of 21°, which is significantly higher than those of EM-1 and EM-3. The peel ply, the release film, the breather and the vacuum bag seem to have slipped, under the pressure of 7 bars, into the area of the radius of curvature during the curing of the sample, thus inducing involuntary wrinkles. The scattering of the wrinkles created for this batch was relatively large, with a standard deviation of 5.5°. The EP-1/8 batch specimen had an average of 26.4° of misalignment angle. The layers with wrinkles were principally the $[45_2/-45_2]$ localised in the lower part of the specimen for the same reasons as explained for the EM-2 specimens. Nevertheless, the central plies at 0° were lightly impacted by the wrinkles induced by the draping strategy, but they were offset from the centre of the radius of curvature.

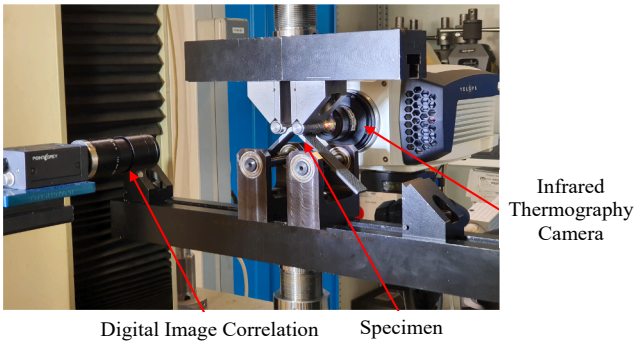

Fig. 6. Setup of the four-point bending test. (For interpretation of the references to colour in this figure legend, the reader is referred to the web version of this article.)

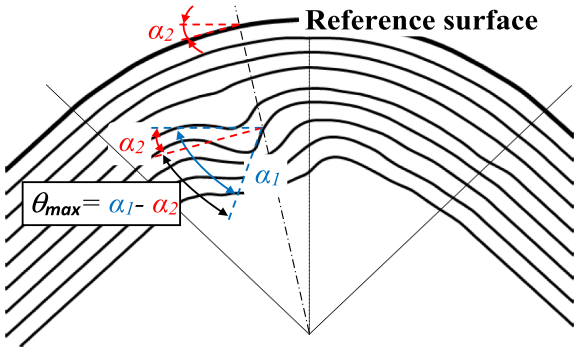

Fig. 7. Measure of the maximum misalignment angle. (For interpretation of the references to colour in this figure legend, the reader is referred to the web version of this article.)

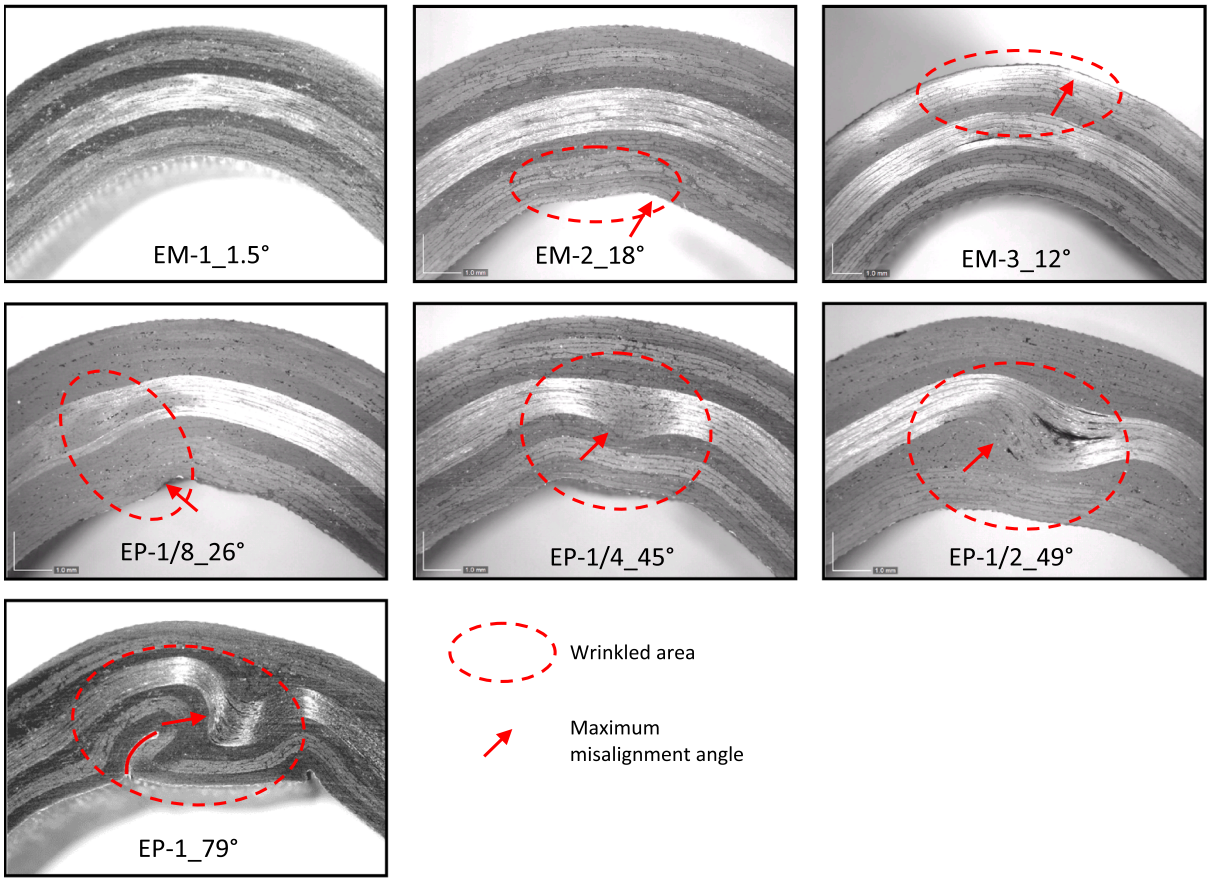

Fig. 8. Example of wrinkles introduced in each batch of specimens. (For interpretation of the references to colour in this figure legend, the reader is referred to the web version of this article.)

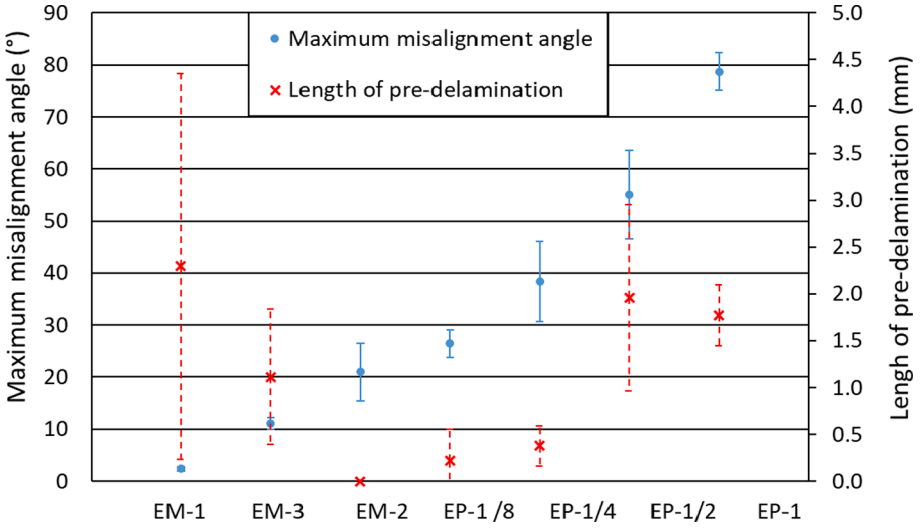

Fig. 9. Distribution of mean values of the maximum misalignment angle and the length of pre-delamination for each batch of specimens. (For interpretation of the references to colour in this figure legend, the reader is referred to the web version of this article.)

Concerning the EP-1/4, EP-1/2 and EP-1 samples, the wrinkles seemed to be induced by the strategy of hand layup described earlier. The plies stacked on a flat surface before being introduced into the concave mould were subject to wrinkling, and so were all the plies stacked into the mould after them. It was observed that increasing the number of plies stacked on a flat surface increased the mean value of maximum misalignment angle with 38.4° for EP-1/4, 55.1°for EP-1/2 and 78.7°for EP-1. Moreover, EP-1/4 and EP-1/2 samples presented a greater scattering than the EP-1. Some voids were present in the EP-1/2 and EP-1 specimens, due to the high level of wrinkles located at the interface of 0° plies and at the interface between 0° and 90° plies in the lower part of the L-angle specimen in the case of EP-1/2. A piece of peel ply (symbolised in red on Fig. 8) was trapped under a wrinkle of the EP-1 specimens, consequently preventing the adhesion of the two inner parts

of the wrinkles and creating a large defect.

To sum up, the aim of this work was to produce specimens with different values of misalignment. Thanks to the two strategies presented previously, seven batches, each of them composed of six curved specimens, were manufactured with a large range of maximum misalignment angles, extending from 1.5 ± 2° to 83 ± 2° in the radius part of the samples (Fig. 9). Therefore, the effect of defects (wrinkles and initial delamination defects) on the mechanical properties will be studied in the next section. The distribution of measured misalignment angle and length of pre-delamination through the width of the sample (Fig. 5) were studied but no trend was identified.

3.2. *Damage scenario of three levels of misalignment angle specimens under four-point bending test*

The first part concerns an L-angle specimen from the EM-1 sample batch, which was taken as a reference for this study because it was the batch of samples with the lowest level of misalignment angle.

The second part deals with an intermediate level of misalignment angle. The sample comes from the EP-1/8 batch of L-angle specimens and has a maximum misalignment angle of 26° relative to the reference surface of the specimen.

The third part looks at a higher level of maximum misalignment by using an EP-1/4 specimen with an angle of misalignment of 45°.

3.2.1. *Maximum misalignment angle of 1.5 ± 2°*

This first L-angle specimen was taken as a reference in this study because it was from the batch of specimens with the lowest level of misalignment angle.

The experimental load-machine displacement envelope curve (formed by the maximum and minimum values of experimental loads and machine displacements) is plotted in Fig. 10 and that corresponding to the specimen studied subsequently is highlighted in blue on the graph. The stiffness of this batch of specimens subjected to the four-point bending test shows low variability and non-linear elastic behaviour with a stiffening in the first part of the tests, as already pointed out in [37]. The different experimental curves exhibit a similar damage scenario with a principal load drop at approximately 5 mm of machine displacement, followed by a succession of load reactions up to 10 mm. The blue curve on Fig. 10 corresponds to the specimen EM-1_02, with a maximum misalignment angle of 1.5°.

This specimen underwent a first load drop at 380 N and 5 mm of machine displacement (point (a) on Fig. 10). This first load drop was driven by the interlaminar fracture between the $[90_2/0_2]$ on the lower part of the specimen and by delaminations between 0° plies at the middle of the thickness of the specimen. The initiation of the delamination was probably caused by an out-of-plane excessive tensile stress. Intralaminar damage, within nearby delaminated plies, was not identified by DIC or infrared thermography. Implication of damage initiation was experimentally delicate because interlaminar damage was predominant and more obviously visible than matrix cracking. A numerical/experimental discussion with the Discrete Ply Numerical model [37] will be useful to investigate this point and it will be discussed deeper in a forthcoming paper. The Digital Image Correlation (DIC) made it possible to point out an out-of-plane strain concentration in the 90° ply and at the interface with the 0° top ply (Fig. 11 a). It is important to mention that damage views noted (a), (b) and (c) on Fig. 11 correspond to the points (a), (b) and (c) on the load-machine displacement curve of Fig. 10. Moreover, on Fig. 11, Fig. 13 and Fig. 15, the side A was in mirror symmetry with the side B about the mid plane of the specimen. The infrared thermography revealed that damage propagated on the other side of the specimen with a significant temperature rise of approximately four degrees relative to the rest of the specimen.

Then a second load drop occurred at 370 N, which is really close to the first failure. The infrared thermography indicated that it was caused by the propagation of delamination previously initiated at the same interface (Fig. 11 b).

To finish, the last principal damage was located in the upper part of the specimen. It caused the last load drop and it consisted of delamination between [90/-45] plies, between [0/90] plies and by matrix cracking of the 90° ply (Fig. 11 c).

It should be noted that damage located at the bottom of the stacking sequence, composed of matrix cracking of the +45° ply and delamination at the interface [+45/−45], occurred between damage (b) and damage (c) on Fig. 10. It is not illustrated on Fig. 11 because it had no significant effect on the load-machine displacement curve. The damage scenario was the same for the other specimens of the batch with a first failure located at the middle of the specimen, most often followed by a second load drop – which was the propagation of the first one – and finally damage located on the upper part of the specimen.

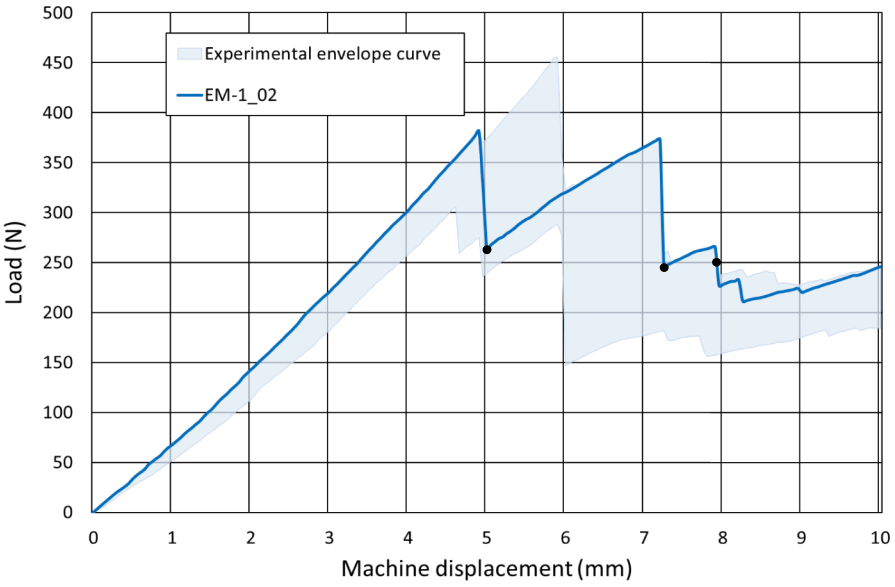

Fig. 10. Load-machine displacement curves of the EM-1 specimens. The experimental envelope curve is formed by the maximum and the minimum values of experimental loads and machine displacements. (For interpretation of the references to colour in this figure legend, the reader is referred to the web version of this article.)

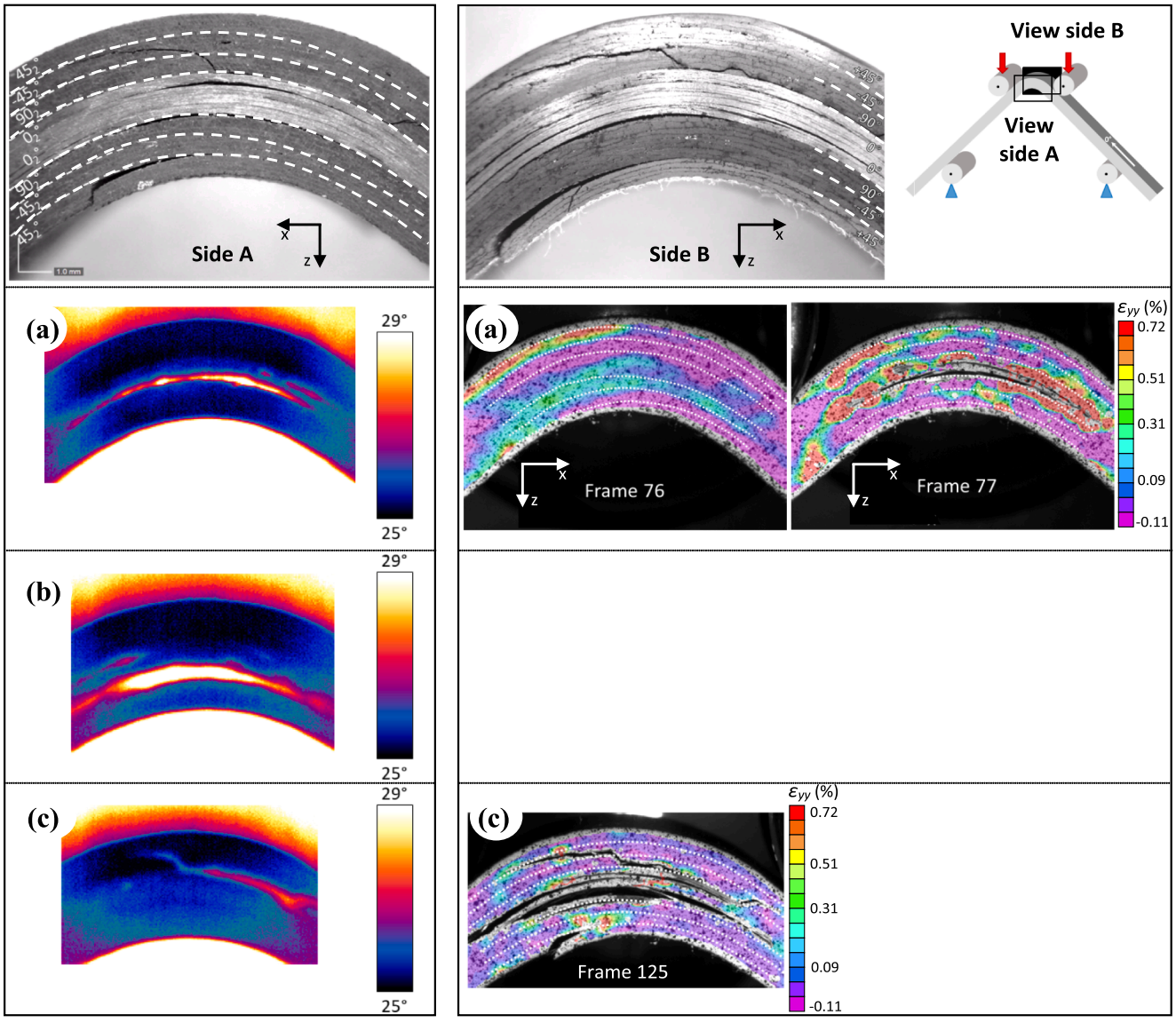

Fig. 11. Damage scenario of the EM-1_02 specimen. In the upper part of the figure, the failed section of sides A and B. On the left of the figure, infrared thermography images and on the right of the figure, the DIC. Damage views noted (a), (b) and (c) correspond to the points (a), (b) and (c) on the load-machine displacement curve of Fig. 10. (For interpretation of the references to colour in this figure legend, the reader is referred to the web version of this article.)

3.2.2. *Maximum misalignment angle of 26 ± 2°*

This second L-angle specimen was chosen with a medium misalignment angle of 26 ± 2°, localised by a red circle on Fig. 13. It must not be forgotten that side A was in mirror symmetry with side B about the mid plane of the specimen. As for Fig. 11, the experimental envelope curve is in light blue and the curve corresponding to that studied in this part is in blue (Fig. 12). The curves show a non-linear elastic behaviour with very low variability and a load reaction lower than in the previous case.

Damage caused by the first load drop at 290 N and 4.4 mm of machine displacement was composed of delaminations between plies [90/0] on faces A and B and by matrix cracking of the 90° ply. On side B, the matrix cracking of the 90° ply spread as far as the interface with the −45° ply (Fig. 13. a). The DIC indicates a stress concentration at this interface [90/0] and, more precisely, on the area where the misalignment angle was the largest. Therefore, the wrinkle played a major role in the failure scenario of this L-angle specimen. The infrared thermography camera showed damage at the same location but it was delamination and a small amount of matrix cracking.

Damage located at the bottom of the stacking sequence (circled in black on Fig. 13. b) was matrix cracking of the 45° ply, and delamination of the ±45° interface had a slight impact on the load-machine displacement curve.

The next damage highlighted was at 235 N and 7 mm of machine displacement (Fig. 13. c). It corresponded to an interlaminar failure between the 0° plies. This delamination initiated the propagation of damage into the upper part of the specimen (failure point d) corresponding to delamination at the [0/90] interface and the [90°/−45°] interface, and to intralaminar matrix cracking within the 90° ply.

Finally, this damage propagated to side B of the specimen, and is indicated by point (e) on the load-machine displacement curve (Fig. 12).

3.2.3. *Maximum misalignment angle of 45 ± 2°*

The experimental envelope curve of load-machine displacement is plotted on Fig. 14. The blue curve corresponds to the experimental results for the EP-1/4_45° specimen studied in this section. The maximum angle of misalignment was localised at the [90/0] interface in the lower part of the specimen and is circled in red on Fig. 15. It should be noted that the variability of the non-linear elastic behaviour was considerably

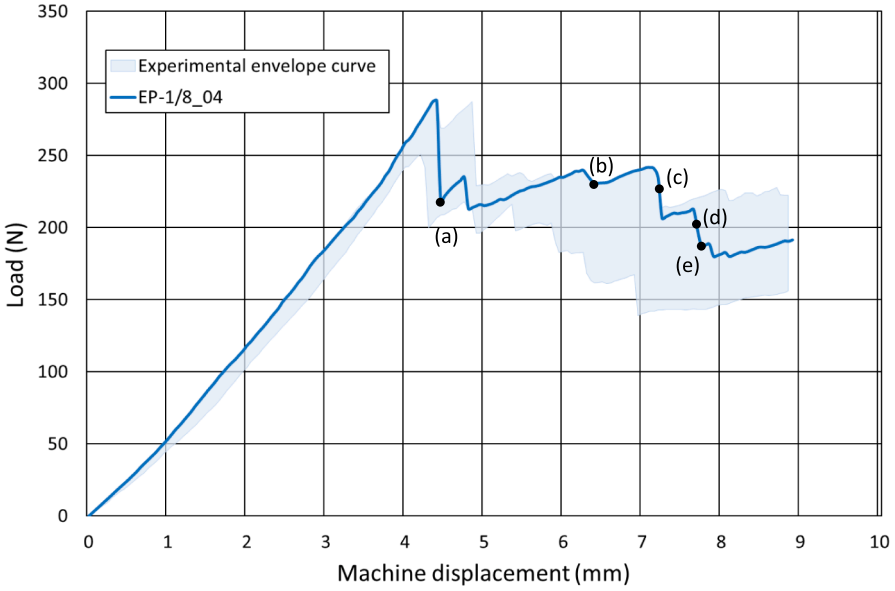

Fig. 12. Load-machine displacement curves of the EP-1/8 specimens. The experimental envelope curve is formed by the maximum and the minimum values of experimental loads and machine displacements. (For interpretation of the references to colour in this figure legend, the reader is referred to the web version of this article.)

lower than in the previous specimen, which was itself lower than the variability of the first specimen studied, with the smallest wrinkles. The presence of wrinkles and the rise of the maximum angle of misalignment seems to localise damage through the specimen, which tends to reduce the variability of the elastic behaviour of the specimen.

On the load-machine displacement curve, a small drop can be seen at 260 N and for a displacement of 4.1 mm. This must be due to damage inside the specimen, but nothing appears on the infrared camera image or on the DIC.

The loading continues with the same stiffness to the first significant load drop (point (a) on Fig. 14) at 310 N and 5 mm of machine displacement, which corresponds to the initiation of damage before an abrupt failure. The infrared thermography camera reveals, on side A of the specimen, a matrix crack inside the 90° ply on the lower part of the specimen. Thanks to the DIC on side B of the specimen, this was found to correspond to a strain concentration at the interface [90/0] (Fig. 15. a) near the maximum of misalignment angle of 45 ± 2° but without damage on this side.

Then the propagation of the damage initiated led to the main load drop of 100 N (point (b) on Fig. 14). This was composed of delamination at the [90/0] interfaces and [−45/90] plies, and matrix cracking of the 90° ply in the lower part of the specimen. Moreover, on side A of the specimen, the infrared thermography camera showed a delamination between +45° and −45° plies.

The last damage occurred at 180 N and 6.5 mm of machine displacement in Fig. 14. It corresponded to the propagation of damage on the upper part of the specimen as previously highlighted for the other specimens. It consisted of delamination at the [90/−45] and [0/90] interfaces and by matrix cracking of the 90° ply. This damage crossed the width of specimens, so there was the same damage on both sides, A and B.

3.3. Analytical calculation of out-of-plane tensile stress without defects

Out-of-plane tensile stress was calculated analytically and compared to the theoretical value of the transverse tensile strength employed by the model used in a previous work [37]. This model was tested and validated with experimental results by its use on four stacking sequences. It provides a highly representative load-machine displacement curve between experiment and numerical simulations.

Through-thickness tensile strengths were analytically calculated according to Eqs. (1)-(3) taken from the ASTM D6415/D3415M-06a standard [38]. σ_r^{max} corresponds to the out-of-plane stress at the first load drop in the load-displacement curve and was calculated from Eq. (4).

$$CBS = \left(\frac{P}{2wcos\phi}\right)\left(\frac{d_x}{\cos\phi} + (D+t)\tan\phi\right) \tag{1}$$

$$\phi = sin^{-1}\left(\frac{-d_x(D+t) + d_y\sqrt{d_x^2 + d_y^2 - D^2 - 2Dt - t^2}}{d_x^2 + d_y^2}\right) \tag{2}$$

$$d_y = d_x tan\phi_i + \frac{D+t}{cos\phi_i} - \Delta \tag{3}$$

$$\sigma_r^{max} = \frac{3 \bullet CBS}{2t\sqrt{r_i r_o}} \tag{4}$$

where CBS is the Curved Beam Strength, $P = 650$ N is the failure load, ϕ is the angle of the specimen legs from the horizontal in degrees, $\phi_i = 45^\circ$ is the angle of the specimen legs from the horizontal in degrees at the beginning of the test, $w = 20$ mm is the width of the specimen, $d_x = 17.9$ mm and $d_y = 35.8$ mm are respectively the horizontal and vertical distances between two adjacent top and bottom loading bars, $t = 4.125$ mm is the theoretical thickness of the specimen, $D = 14$ mm is the diameter of the cylindrical loading bars, $r_i = 5.16$ mm and $r_o = 9.29$ mm are respectively the inner and outer radii, $\Delta = 7.75$ mm corresponds to the imposed displacement at failure. Failure load P and imposed displacement Δ at failure were determined thanks to simulation on a pristine specimen performed with a previous model presented in [37] for four-point bending tests on curved specimens without defects. This model finds the maximal load and displacement at failure.

The out-of-plane tensile stress determined with the analytical equations (Eq. 1) – (Eq. 4) was $\sigma_r^{max} = 37.9$ MPa. This is different from the value of 50 MPa, which corresponded to the transverse tensile strength of the T700/M21 used and validated with the Discrete Ply Model used in [37]. This model is based on a full 3D modelling accurately taking into account inter and intralaminar coupling. This model is probably less

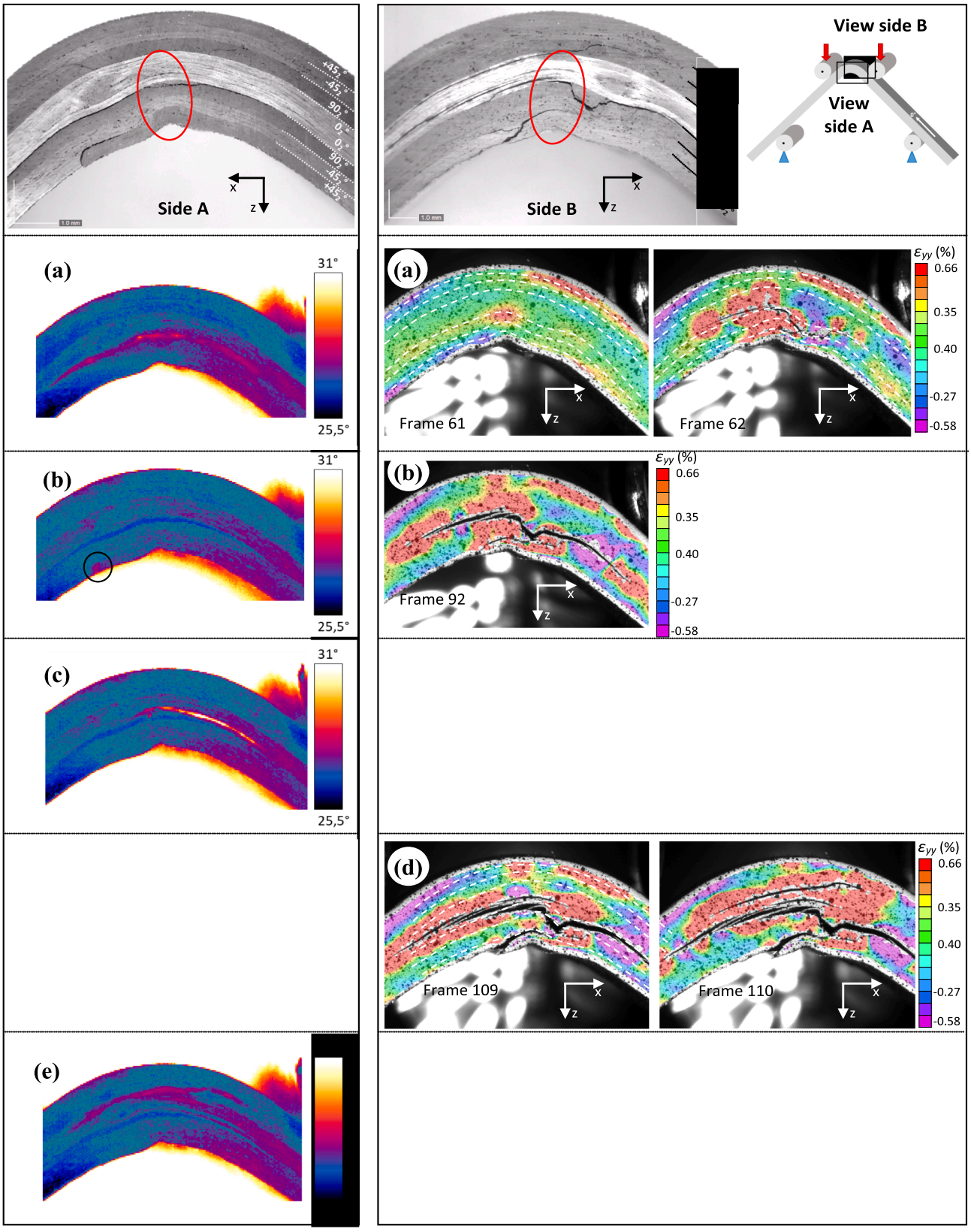

Fig. 13. Damage scenario of the EP-1/8_04 specimen. In the upper part of the figure, the failed section of side A and side B. On the left of the figure, infrared thermography images and, on the right of the figure, the DIC. Damage views noted (a), (b) and (c) correspond to the points (a), (b) and (c) on the load-machine displacement curve of Fig. 12. (For interpretation of the references to colour in this figure legend, the reader is referred to the web version of this article.)

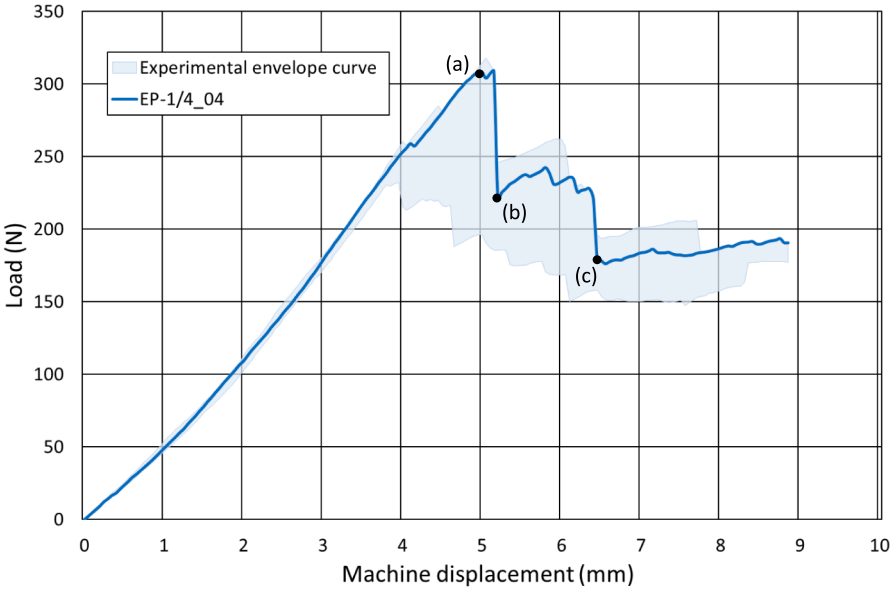

Fig. 14. Load-machine displacement curves of the EP-1/4 specimens. The experimental envelope curve is formed by the maximum and the minimum values of experimental loads and machine displacements. (For interpretation of the references to colour in this figure legend, the reader is referred to the web version of this article.)

conservative than the analytical method. In particular, the appearance of matrix cracking in the 90° plies delay the delamination as showed in [37]. In addition, experimental investigations shown experimental matrix cracking in internal 90° ply, which was not taking into consideration by the ASTM standard and could also explain this difference. Moreover, another source of discrepancy may be due to the limitation by the ASTM standard [38] to a maximum displacement of the roller of 5 mm, which is not respected here. Based on the results given by the model in [37] a failure load of 650 N was assumed and was considered as the theoretical reference for the pristine specimen in the rest of this work.

3.4. Comparison of failure loads for different levels of maximum misalignment angle

The evolution of the failure loads according to the maximum misalignment angle for the 42 L-angle specimens tested in this study is presented in Fig. 16. Each batch of specimens has been circled so as to be identified on the graph.

It should be noted that, for batch EM-1, the variably of failure loads was relatively large, with values of failure load spread over 130 N. This variability could be explained by the presence of pre-delamination (before the test) between two plies at 0° in some specimens. This is clearly visible on the specimen of Fig. 17 but pre-delamination was not visible in all specimens of the batch EM-1. The length of pre-delamination corresponds to the average of the measurements on both sides of each specimen. The lengths of pre-delamination are plotted in Fig. 18 for the six specimens of the batch EM-1. They have high variability of pre-delaminated length, spread over 5 mm. In this case, this parameter did not allow any conclusions to be drawn concerning the evolution of the failure loads. The most interesting parameter may have been the pre-delaminated surface area. Nevertheless, this batch of specimens showed strong repeatability value of the maximum misalignment angle.

Most specimens (EM-2, EP-1/8, EP-1/4, EP-1) have a pre-delaminated length range smaller than 1 mm, unlike EM-3 and EP-1/2, which have a length range spread over 2.5 mm (Fig. 18). This is half that of the EM-1 batch. The EM-3 specimens show good repeatability concerning the failure load, with a range spread over 30 N. Only two points referring to batch EM-3 were outside the average: the first with a length of 0 mm and the other with a length of 2 mm (Fig. 18). Points with a length of pre-delamination equal to 0 mm were moved slightly towards the vertical axis to distinguish the different points better. This means that the points were not representative of the rest of the batch. Concerning the EP-1/2 specimens, the evolution was relatively more extended over the range and this batch had values of failure loads spread over a range of 60 N. Nevertheless, as for the EM-1 batch, the evolution of pre-delaminated length did not highlight any relation between the length of pre-delamination and the failure load. To finish, the EM-2 batch had a range of failure loads spread over 100 N but no problems of initial delamination were visible on the images of each side face of the specimens.

In conclusion, this parameter did not reveal any relation between the failure load and the length of pre-delamination, since the measurements on each of the side faces of the specimens did not provide an acceptable estimation of the real state of the structure. A more interesting parameter could have been the pre-delaminated surface area. Finally, a parameter coupling the maximum misalignment angle with the area of pre-delamination should be considered to characterise the link between the amount of defects and the drop of failure load.

The graph depicting the evolution of the failure load compared to the maximum misalignment angle, Fig. 16, clearly indicates a trend for the failure load to decrease with the rise of the maximum misalignment angle – except for the EP-1/2 specimens, with their failure load average of 360 N, which was higher than for the other specimens with a minimum angle of misalignment of 10°. These results mean that other parameters could be involved in the failure of this batch of specimens. For example, modification of the general shape of the specimen (on the region of the radius of curvature), the presence of defects: wrinkles and pre-delaminated areas at specific locations inside the sample, could be the cause of interlaminar stress relaxation within the structure and have a beneficial effect on the breakage, thus tending to increase the structure's strength.

Fig. 19 presents the evolution of the normalised failure loads according to the maximum misalignment angles for different types of tests found in the literature. A qualitative analysis is proposed in the purpose of making a first comparison on the effect of wrinkles on the strength of composite structures. The aim of this first approach is to identify the configuration (shape + loading) with the maximum effect of defect.

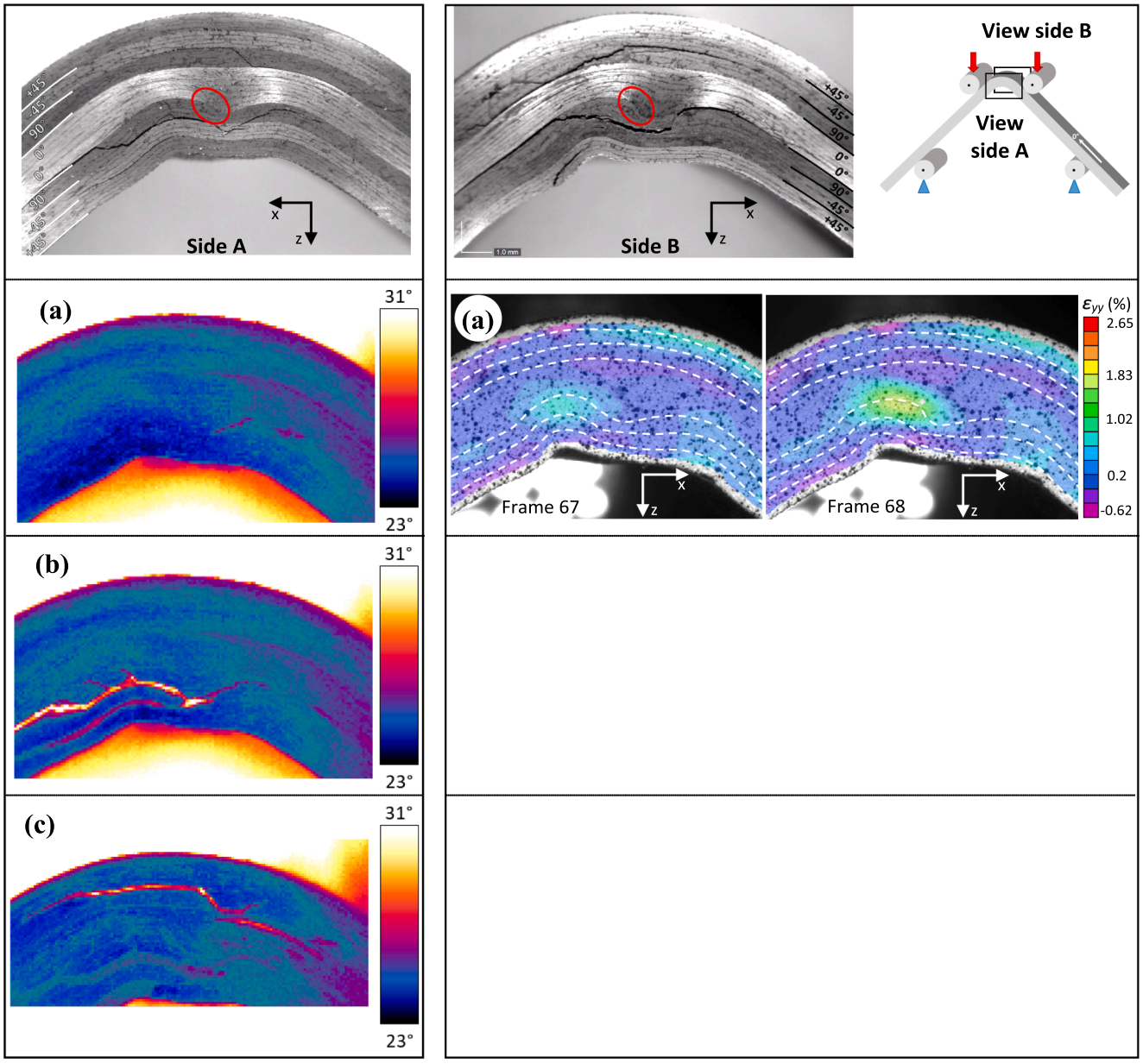

Fig. 15. Damage scenario of the EP-1/4_04 specimen. In the upper part of the figure, the failed section of sides A and B. On the left of the figure, infrared thermography images and, on the right of the figure, the DIC. Damage views noted (a), (b) and (c) correspond to the points (a), (b) and (c) on the load-machine displacement curve of Fig. 14. (For interpretation of the references to colour in this figure legend, the reader is referred to the web version of this article.)

Mukhopadhyay et al. have tested flat specimens with embedded wrinkles in quasi-isotropic $[45_2/90_2/-45_2/0_2]_{3s}$ staking sequence. They used Hexcel's IM7/8552 pre-preg with a nominal cured thickness of 0.125 mm, which lead to a total thickness of 6 mm. They manufactured specimens with three levels of misalignment angle and tested their flat specimen under tensile [39] and compressive [24] tests. Specimens have respective dimensions of 250 mm × 30 mm × 6 mm (with a gauge length of 150 mm) and 110 mm × 30 mm × 6 mm (with a gauge length of 30 mm). The three levels of maximum misalignment angle was similar for specimens tested under tensile (4.9°, 8.8° and 12.1°) and compressive tests (5.6°, 9.9° and 11.4°). Xu et al. [33] tested quasi-isotropic curved specimen made from IM7/8552 pre-preg under four point bending test. Specimens presented an inner radius of 20 mm, a total thickness of 9.25 mm and a maximum misalignment angle of 18°. Finally, Hu et al. [34] have tested curved quasi-isotropic specimens under bending test. AS4/8552 pre-preg was considered to manufacture specimens. They presented a total thickness of 16.14 ± 0.2 mm and an inner radius of approximately 14 mm. It is noteworthy that Hu et al. [34] did not measured and used the maximum misalignment angle to characterise wrinkles. Hence, it were estimated from the data available in the article, which generated a large discrepancy. Configurations tests were assumed to be different, for these reasons and to be compare the failure load was normalised relative to the failure load of each pristine specimen.

The knockdown factor obtained by Xu et al. [33] and Hu et al. [34] was significantly different. Nevertheless, it is important to remember that Xu et al. [33] manufactured specimens with an embedded wrinkle through the thickness, obtained by adding transversal strips, and the total thickness of their sample was approximately twice that of the specimens studied in this work. The knockdown factor found by Hu et al. [34] was clearly higher than the one produced by Xu et al. [33]. It was very close to the knockdown factor found by Mukhopadhyay et al. [24] on flat specimens with out-of-plane embedded wrinkles under compressive tests. Mukhopadhyay et al. [39] also tested their specimens under tensile stress [39] and the Knockdown factor was lower than on

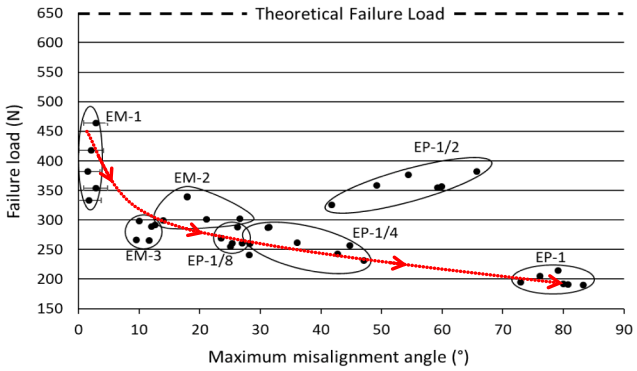

Fig. 16. Evolution of failure load according to the maximum misalignment angle. (For interpretation of the references to colour in this figure legend, the reader is referred to the web version of this article.)

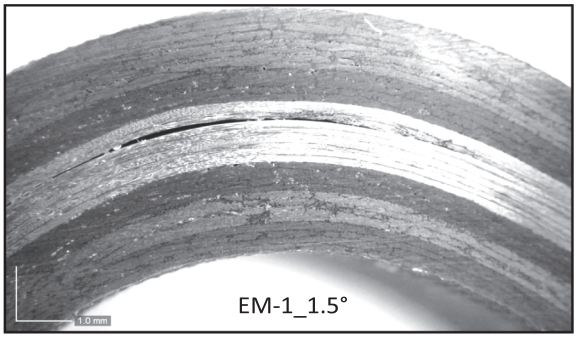

Fig. 17. Example of EM-1 specimen with presence of initial delamination.

the specimen in compressive tests. In conclusion, the decrease induced by the presence of wrinkle defects was greater in the case of the four-point bending test than in tensile and compressive tests, which seems logical considering the geometry of the specimen and the type of load applied. In the case of bending tests on L-shaped specimens, out-of-plane stresses were significantly higher than on in-plane tests.

4. Conclusions

Seven batches of 6 specimens were produced for this study and two hand layup strategies were used to manufacture samples with different levels of wrinkles, using convex and concave moulds. Increasing the number of plies previously stacked on a flat surface before being introduced into the mould increased the maximum misalignment angle of the specimens, from 1.5° to 83°.

For each of the detailed levels (1.5°, 26° and 45°), the damage scenario was similar, with first damage composed by a delamination at the interface [0/90] and localised in the lower part of the specimen, which is in agreement with [27,35,40]. In the case of the intermediate and pronounced wrinkles, matrix cracking in the 90° ply was also noticed. The DIC showed a strain concentration near the maximum misalignment angle. The wrinkle localised damage and spread it through the thickness of the specimen via matrix cracking. Each curve presented a reacting load after the first load drop. Only for the lowest level of misalignment did the reacting load increase to the same value as before the first load drop. Then, delamination and matrix cracking spread into the lower part of the sample before causing the last major load drop induced by damage in the upper part of the structure. This damage was composed of delamination at the [90/−45] and [0/90] interfaces and matrix cracking of the 90° plies, which was localised between these two delaminated interfaces. In the case of EM-1, with the lowest level of misalignment, the damage also included delamination of the [−45/45] interface and matrix cracking was also present in the −45° ply. These damage scenarios were in agreement with the results presented by [35] on the study of L-angle shapes without wrinkles under four-point bending tests.

It can be noted that the effect of wrinkle defects was clearly greater on curved specimens under four-point bending tests than on flat specimens under tensile or compressive tests (Fig. 19). The knockdown factor corresponding to a four-point bending test for a specimen with a misalignment angle of approximately 1.5 ± 2° is about 36%, while it was only 18% and 4% for compressive and tensile tests, respectively on specimens with a misalignment angle of 5.6°. In the case of specimens with a misalignment angle of 10°, the knockdown factor was 55%, 33% and 14% for four-point bending, compressive and tensile tests, respectively. This value could seem remarkably high but it was reasonable because, in the case of the four-point bending test, the wrinkles were localised in a single area, in the curved part of the specimen. As seen in the introduction, this zone is more subject to wrinkle defects than flat parts. In addition, under four-point bending loads, stresses are

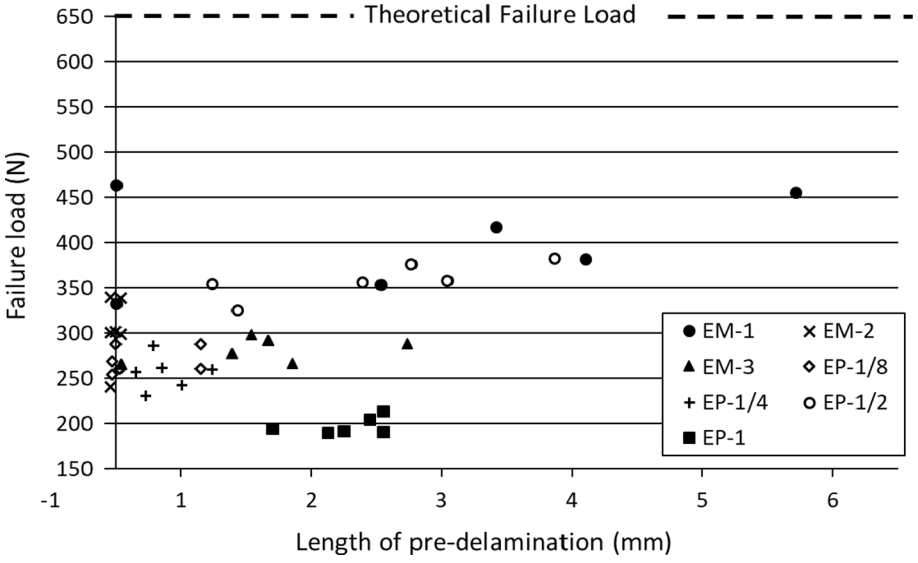

Fig. 18. Length of pre-delamination for all the specimens.

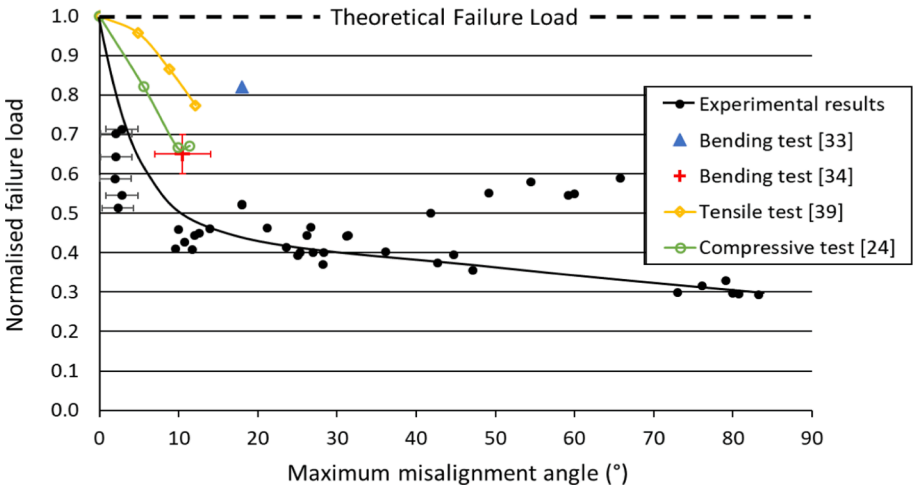

Fig. 19. Comparison of the evolution of normalised failure loads according to maximum misalignment angles for different types of tests. Values symbolised by black dots correspond to the experimental results of this study. Values symbolised by the blue triangle and the red cross correspond to the experimental results of [33] and [34], respectively. Values represented by yellow diamond and green circles correspond to the experimental results of [39] and [24], respectively. (For interpretation of the references to colour in this figure legend, the reader is referred to the web version of this article.)

concentrated in the radius of curvature and are principally out-of-plane compared to tensile and compressive tests on flat specimens, which can explain such large differences of knockdown factors. Nevertheless, knockdown factors found by Xu et al. [33] and Hu et al. [34] in their studies were relatively different from the knockdown factors proposed in this work. That could be explained by a huge difference of the thickness of the specimen, which was at least twice that of the thickness of the specimen studied here.

As for the Barely Visible Impact Damage used in damage tolerance of aeronautic structures, there is probably a link between the external shape (modification of the internal radius and the variation of the thickness in the curved part) and the maximum misalignment angle. This link should be identified by deeper investigation on a larger number of specimens.

CRediT authorship contribution statement

P. Journoud: Investigation, Methodology, Validation, Writing – original draft. **C. Bouvet:** Conceptualization, Supervision. **B. Castanié:** Conceptualization, Supervision, Writing-review & editing. **L. Ratsifandrihana:** Project administration, Conceptualization.

Declaration of Competing Interest

The authors declare that they have no known competing financial interests or personal relationships that could have appeared to influence the work reported in this paper.

References

[1] Castanie B, Bouvet C, Ginot M. Review of composite sandwich structure in aeronautic applications. Compos Part C Open Access 2020;1:100004. https://doi.org/10.1016/j.jcomc.2020.100004.

[2] Neveu F, Castanié B, Olivier P. The GAP methodology: A new way to design composite structures. Mater Des 2019;172:107755. https://doi.org/10.1016/j.matdes.2019.107755.

[3] Hassan MH, Othman AR, Kamaruddin S. A review on the manufacturing defects of complex-shaped laminate in aircraft composite structures. Int J Adv Manuf Technol 2017;91:4081–94. https://doi.org/10.1007/s00170-017-0096-5.

[4] Potter KD, Langer C, Hodgkiss B, Lamb S. Sources of variability in uncured aerospace grade unidirectional carbon fibre epoxy preimpregnate. Compos Part A Appl Sci Manuf 2007;38:905–16. https://doi.org/10.1016/j.compositesa.2006.07.010.

[5] Lerman MW. Investigation of the effect of in-plane fibre waviness in composite materials through multiple scales of testing and finite element modelling. MSc Thesis, Montana State University Montana, United States. n.d.

[6] EL -Hajjar R, Grant P, Ashforth C. Composite Structures. Effect of Defects. John Wiley and Son, Chichester, West Sussex, UK; 2019.

[7] Potter KD, Khan B, Wisnom MR, Bell T, Stevens J. Variability, fibre waviness and misalignment in the determination of the properties of composite materials and structures. Compos Part A Appl Sci Manuf 2008;39:1343–54. https://doi.org/10.1016/j.compositesa.2008.04.016.

[8] Kulkarni P, Mali KD, Singh S. An overview of the formation of fibre waviness and its effect on the mechanical performance of fibre reinforced polymer composites. Compos Part A Appl Sci Manuf 2020;137:106013. https://doi.org/10.1016/j.compositesa.2020.106013.

[9] Johnson KJ, Butler R, Loukaides EG, Scarth C, Rhead AT. Stacking sequence selection for defect-free forming of uni-directional ply laminates. Compos Sci Technol 2019;171:34–43. https://doi.org/10.1016/j.compscitech.2018.11.048.

[10] Li Y, Li M, Gu Y, Zhang Z. Numerical and experimental study on the effect of lay-up type and structural elements on thickness uniformity of L-shaped laminates. Appl Compos Mater 2009;16:101–15. https://doi.org/10.1007/s10443-009-9080-z.

[11] Potter KD. Understanding the origins of defects and variability in composites manufacture. ICCM Int Conf Compos Mater 2009.

[12] Dodwell TJ, Butler R, Hunt GW. Out-of-plane ply wrinkling defects during consolidation over an external radius. Compos Sci Technol 2014;105:151–9. https://doi.org/10.1016/j.compscitech.2014.10.007.

[13] Rashidi A, Belnoue JPH, Thompson AJ, Hallett SR, Milani AS. Consolidation-driven wrinkling in carbon/epoxy woven fabric prepregs: An experimental and numerical study. Compos Part A Appl Sci Manuf 2021;143:106298. https://doi.org/10.1016/j.compositesa.2021.106298.

[14] Hallander P, Akermo M, Mattei C, Petersson M, Nyman T. An experimental study of mechanisms behind wrinkle development during forming of composite laminates. Compos Part A Appl Sci Manuf 2013;50:54–64. https://doi.org/10.1016/j.compositesa.2013.03.013.

[15] Potter KD, Campbell M, Langer C, Wisnom MR. The generation of geometrical deformations due to tool/part interaction in the manufacture of composite components. Compos Part A Appl Sci Manuf 2005;36:301–8. https://doi.org/10.1016/J.COMPOSITESA.2004.06.002.

[16] Lightfoot JS, Wisnom MR, Potter KD. A new mechanism for the formation of ply wrinkles due to shear between plies. Compos Part A Appl Sci Manuf 2013;49:139–47. https://doi.org/10.1016/j.compositesa.2013.03.002.

[17] Netzel C, Mordasini A, Schubert J, Allen T, Battley M, Hickey CMD, et al. An experimental study of defect evolution in corners by autoclave processing of prepreg material. Compos - Part A Appl Sci Manuf 2021;Volume 144:106348. doi:10.1016/j.compositesa.2021.106348.

[18] Brillant M. Out-of-Autoclave Manufacturing of Complex Shape Composite Laminates. MSc Thesis, McGill University Montreal, Canada, 2010.

[19] Fernlund G, Rahman N, Courdji R, Bresslauer M, Poursartip A, Willden K, et al. Experimental and numerical study of the effect of cure cycle, tool surface, geometry, and lay-up on the dimensional fidelity of autoclave-processed composite parts. Compos Part A Appl Sci Manuf 2002;33(3):341–51.

[20] Hubert P, Poursartip A. Aspects of the compaction of composite angle laminates: an experimental investigation. J Compos Mater 2001;35:2–26. https://doi.org/10.1106/X8D7-PR9V-U6F2-0JEK.

[21] Fernlund G, Griffith J, Courdji R, Poursartip A. Experimental and numerical study of the effect of caul-sheets on corner thinning of composite laminates. Compos - Part A Appl Sci Manuf 2002;33:411–26. doi:10.1016/S1359-835X(01)00114-2.

[22] Dang C, Bernetich K, Carter E, Butler G. Mechanical comparision of out-of-autoclave prepreg part to conventional autoclave prepreg part. American Helicopter Society 67th Annual Forum, Virginia Beach, VA, May 3-5, 2011.

[23] Wang X, Zhang Z, Xie F, Li M, Dai D, Wang F. Correlated rules between complex structure of composite components and manufacturing defects in autoclave molding technology. J Reinf Plast Compos 2009;28:2791–803. https://doi.org/10.1177/0731684408093876.

[24] Mukhopadhyay S, Jones MI, Hallett SR. Compressive failure of laminates containing an embedded wrinkle; experimental and numerical study. Compos Part A Appl Sci Manuf 2015;73:132–42. https://doi.org/10.1016/j.compositesa.2015.07.007.

[25] Arian Nik M, Fayazbakhsh K, Pasini D, Lessard L. Optimization of variable stiffness composites with embedded defects induced by Automated Fiber Placement. Compos Struct 2014;107:160–6. https://doi.org/10.1016/j.compstruct.2013.07.059.
[26] Belnoue J-H, Mesogitis T, Nixon-Pearson OJ, Kratz J, Ivanov DS, Partridge IK, et al. Understanding and predicting defect formation in automated fibre placement pre-preg laminates. Compos Part A Appl Sci Manuf 2017;102:196–206.
[27] Xie N, Smith RA, Mukhopadhyay S, Hallett SR. A numerical study on the influence of composite wrinkle defect geometry on compressive strength. Mater Des 2018; 140:7–20. https://doi.org/10.1016/j.matdes.2017.11.034.
[28] Çinar K, Ersoy N. Effect of fibre wrinkling to the spring-in behaviour of L-shaped composite materials. Compos Part A Appl Sci Manuf 2015;69:105–14. https://doi.org/10.1016/j.compositesa.2014.10.025.
[29] Thor M, Sause MGR, Hinterhölzl RM. Mechanisms of origin and classification of out-of-plane fiber waviness in composite materials — A review. J Compos Sci 2020; 4(3):130.
[30] O'Hare Adams D, Hyer MW. Effects of layer waviness on the compression strength of thermoplastic composite laminates. J Reinf Plast Compos 1993;12(4):414–29.
[31] Hsiao HM, Daniel IM. Effect of fiber waviness on stiffness and strength reduction of unidirectional composites under compressive loading. Compos Sci Technol 1996; 56:581–93. https://doi.org/10.1016/0266-3538(96)00045-0.
[32] Lemanski SL, Sutcliffe MPF. Compressive failure of finite size unidirectional composite laminates with a region of fibre waviness. Compos Part A Appl Sci Manuf 2012;43:435–44. https://doi.org/10.1016/j.compositesa.2011.11.007.
[33] Xu X, Jones MI, Ali H, Wisnom MR, Hallett SR. Effect of out-of-plane wrinkles in curved multi-directional carbon/epoxy laminates. Compos Sci Technol 2020;197: 108282. https://doi.org/10.1016/j.compscitech.2020.108282.
[34] Hu H, Cao D, Cao Z, Li S. Experimental and numerical investigations of wrinkle effect on failure behavior of curved composite laminates. Compos Struct 2021;261: 113541. https://doi.org/10.1016/j.compstruct.2021.113541.
[35] Charrier JS, Laurin F, Carrère N, Mahdi S. Determination of the out-of-plane tensile strength using four-point bending tests on laminated L-angle specimens with different stacking sequences and total thicknesses. Compos Part A Appl Sci Manuf 2016;81:243–53. https://doi.org/10.1016/j.compositesa.2015.11.018.
[36] Charrier JS. Développement de méthodologie dédiées à l'analyse robuste de la tenue de structures composites sous chargements complexe tridimensionnels. PhD Ecole nationale supérieure d'arts et métiers - ENSAM, 2013, Paris, France.
[37] Journoud P, Bouvet C, Castanié B, Laurin F, Ratsifandrihana L. Experimental and numerical analysis of unfolding failure of L-shaped CFRP specimens. Compos Struct 2020;232:111563. https://doi.org/10.1016/j.compstruct.2019.111563.
[38] ASTM D6415/D 6415M -06a. Standard test method for measuring the curved beam strength for fiber reinforced polymer matrix composite, 2006.
[39] Mukhopadhyay S, Jones MI, Hallett SR. Tensile failure of laminates containing an embedded wrinkle; numerical and experimental study. Compos Part A Appl Sci Manuf 2015;77:219–28. https://doi.org/10.1016/j.compositesa.2015.07.007.
[40] González-Cantero JM, Graciani E, López-Romano B, París F. Competing mechanisms in the unfolding failure in composite laminates. Compos Sci Technol 2018;156:223–30. https://doi.org/10.1016/j.compscitech.2017.12.022.